Cement and Concrete Composites 130 (2022) 104562

Contents lists available at ScienceDirect

Cement and Concrete Composites

journal homepage: www.elsevier.com/locate/cemconcomp

Influence of printing parameters on 3D printing engineered cementitious composites (3DP-ECC)

Wen Zhou [a], Yamei Zhang [b], Lei Ma [b], Victor C. Li [a,*]

[a] Department of Civil and Environmental Engineering, University of Michigan, Ann Arbor, MI, 48109, USA
[b] School of Materials Science and Engineering, Southeast University, Nanjing, 211189, PR China

ARTICLE INFO

Keywords:
Engineered cementitious composites (ECC)
3D printing
Mechanical properties
Micro-structure
Printing parameter

ABSTRACT

3D printing of engineered cementitious composites (3DP-ECC) serves as an effective means to enable digital and automated construction while removing the dependence of steel reinforcement typical in normal concrete construction. As generally recognized, process control in 3DP is as crucial as material constituents to the performance of the printed structure. Printing parameters pose direct influence on the micro-structure of material, which further impacts the macro-scale properties of printed ECC. In this paper, the effects of different nozzle standoff distances and nozzle travelling speeds are investigated. It is found that lowering the nozzle standoff distance within a certain range increases the in-plane tensile strength and strain capacity of 3DP-ECC by 39% and 30%, respectively. The tensile performance is also enhanced by a moderate printing speed. In addition, a 141% increase in interfacial fiber bridging force is found with elevated nozzle standoff distance. Furthermore, the micro-structure observed via μ-CT correlates well with the printing parameters, micro-structure and macro-scale properties of 3DP-ECC.

1. Introduction

Extrusion-based 3D concrete printing (3DCP) has revolutionized the traditional construction practices and brought new horizons for the development of the construction sector [1–3]. As an advanced additive manufacturing technology, 3DCP allows the printer to deposit cementitious materials layer by layer according to a predefined digital model, and automatically generate a printed concrete element [3]. With automation procedure, 3D printing transcends the traditional labor-intensive construction mode and economizes on manpower to the greatest extent. The efficiency of construction is also substantially promoted. In addition, additive manufacturing removes the need for formwork required in traditional concrete casting [4], which enables 3DCP to produce geometrically complex elements or structures and realize the unification of both standardization and customization in manufacturing. Furthermore, considering the immense environmental impact of the construction industry (approximately 38% of global greenhouse gas emissions and 40% of solid waste generation) [1,5,6], the significance of reduction in material input and construction wastes is far from trivial [7].

Although 3DCP has rendered concrete constructions broader possibilities, concrete has its inherent limitations as a building material, especially when it is applied in the 3DCP process. Generally, concrete fails in a brittle or quasi-brittle mode under load. To avoid catastrophic structural failure, steel reinforcement is necessary in traditional practice [8]. Unfortunately, steel reinforcement is usually incompatible with 3DCP [9], which substantially impedes the development and practical application of 3DCP technology, especially in large scale construction.

To solve the intrinsic conflict between the need of steel reinforcement and the practice of 3DCP, cementitious material with high ductility has been considered a promising substitute for conventional concrete as the printing ink. Engineered cementitious composites (ECC) exhibit strain-hardening characteristics and considerable tensile ductility, which distinguish ECC from conventional concrete and ordinary fiber reinforced concrete (FRC). For FRC loaded under uniaxial tension, deformation localization occurs at the first and only crack site, while overall load carrying capacity drops. This tension-softening behavior in FRC is valued for its more gradual loss of strength and its ability to limit the width of cracks by the bridging fibers (Fig. 1a). Instead of tension-softening, ECC undergoes strain-hardening and continues to bear higher loads at increasing imposed strain, as shown in Fig. 1b. The growing tensile deformation in ECC is not localized but spreads to multiple micro-cracks covering an enlarging specimen volume. The

* Corresponding author.
E-mail addresses: wzhoucee@umich.edu (W. Zhou), ymzhang@seu.edu.cn (Y. Zhang), 230198608@seu.edu.cn (L. Ma), vcli@umich.edu (V.C. Li).

https://doi.org/10.1016/j.cemconcomp.2022.104562
Received 7 January 2022; Received in revised form 16 March 2022; Accepted 23 April 2022
Available online 27 April 2022

multiple micro-cracking process represents a volumetric inelastic strain deformation analogous to plastic yielding of a ductile metal [10]. This self-reinforcing feature of ECC removes the dependence on steel reinforcement, making ECC an attractive ink for 3D printing [9].

To date, successful experiences have been gained in printing ECC components. Li et al. [9] and Yu et al. [11] reported a stable twisted column with a height of 1.5 m and 150 layers printed, clear of structural collapse or material failure. Zhu et al. [12] also obtained hollow ECC cylinders with 17 layers. In the experiments by Figueiredo et al. [13], the printed ECC element eventually collapsed at the 14th layer. Various ECC mix designs (with different fiber content, sand-to-binder ratios and water-to-binder ratios) were studied by Ogura et al. [14]. Mixtures with sufficient static yield stress and leading to no considerable deformation at the bottom layer was optimized for printing wall elements up to 120 mm high. However, the current focus on 3DP-ECC is mainly on mix design, feasibility study, and basic mechanical properties. The significance of process parameters has not yet received due attention.

The contribution of appropriate printing parameters to successful printing has long been recognized in the context of 3DP conventional concrete. The most decisive parameters include nozzle travelling speed, material extrusion rate, nozzle standoff distance, layer cycling time, nozzle shape and size, etc. [3,15–20]. These parameters pose substantial impacts on the extruding and stacking process in the early stage of 3DP life cycle and also on the properties of the resulting element. For instance, a controlling factor of extrudability is the synchronization between travelling speed of the nozzle and flow rate of the extruded material. The flow rate should accurately sync up with the nozzle movement, otherwise the printed filament will exhibit discontinuity or inconsistency [15,21]. Furthermore, the determination of travelling speed requires careful considerations. If the horizontal printing speed is excessively increased, the inertia-induced stress in the extruded material cannot be neglected. Therefore, rapid deposition may cause geometric defects in the extruded cross-section [3,17]. Another example is how nozzle standoff distance affects printing. It is suggested for 3DCP that a proper choice of nozzle standoff distance, i.e., the height of the nozzle above the upper surface of previous layer, can alleviate the problem of insufficient interface bonding [22]. Experiments have shown that reducing the standoff distance to approximately or slightly below the filament thickness suppresses the appearance of large voids at the interface [23,24]. However, such pressing may cause uncontrolled geometric deviations and additional stress burdens to the underlying layer, even resulting in instability failures during the build-up process [25].

Despite the attention that process parameters received in the field of traditional 3DCP, as stated above, no research on printing parameters of 3DP-ECC has been reported. However, such research is necessitated by the features of ECC. The rheology of ECC containing a relatively high content (up to 2% by volume) of microfibers with diameter less than 40 μm creates unique processing challenges, and sparks interest in the impact of printing processes on its self-reinforcing features. In addition, interlayer properties of 3DP-ECC needs to be investigated to understand the influence of fiber bridging on the interface fracture resistance to loading.

To fill the research gap, this article aims at investigating the interrelations among material production control (printing parameters), micro-structure and macro-scale properties of 3DP-ECC. As conceptually illustrated in Fig. 2, with material constituents held constant, the adjustment of printing parameters is reflected by the variation in micro-structure of 3DP-ECC, which further poses influence on the material properties. In turn, the properties measured at macro-scale serve as feedbacks on the process control of 3DP-ECC. In this paper, focus is placed on varying the nozzle travelling speeds and nozzle standoff distances. The resulting micro-structure of 3DP-ECC was observed through micro computed tomography scanners (μ-CT). Further, tensile performance and interlayer fracture performance of printed ECC were evaluated using uniaxial tensile tests and three-point bending tests.

2. Experimental programs

2.1. Materials and mixing procedure

The binders used include ordinary Portland cement 42.5R, fly ash and silica fume, the chemical compositions of which are listed in Table 1. Silica sand with a particle size ranging from 100 μm to 200 μm was adopted for fine aggregate. Polyethylene (PE) fibers with a length of 12 mm were used as reinforcement of ECC. The properties of PE fibers are summarized in Table 2.

The two mix proportions of PE-ECC are listed in Table 3. Mix-1 was designed only for purpose of comparison regarding rheological properties, while Mix-2 was adopted for 3D printing in the following tests and casting of control (non-printed) specimens. The water-to-binder ratios of Mix-1 and Mix-2 are 0.22 and 0.24, respectively. The sand-to-binder ratio is 0.29 for both. The dosage of PE fiber is 1.5% by volume of the total composition. Using Mix-2 composition, mold-cast PE-ECC was tested. The cube compressive strength of cast ECC is 63.3 MPa with a 40 mm × 40 mm × 40 mm specimen. The flexural strength obtained from a 40 mm × 40 mm × 160 mm specimen is 14.8 MPa.

In preparation of the printing ink, all the dry ingredients, i.e., binders, sand and powdery SP, were premixed for 1 min first. Then 90% of the mixing water was added and agitated for 2 min to liquefy the dry materials. Fibers were divided into three equal portions and added to the mixture separately with an interval of 3 min's mixing each time. To promote the viscosity of the mortar before fiber addition and enhance uniform fiber dispersion [26], the remaining water was held back until all the fibers were properly dispersed. The mixing speed was kept at 48 rpm during the mixing process. The fresh mixture of PE-ECC was transferred directly from the mixer to the material hopper of 3D printer at the time of 20 min after addition of the first batch of water. Fig. 3

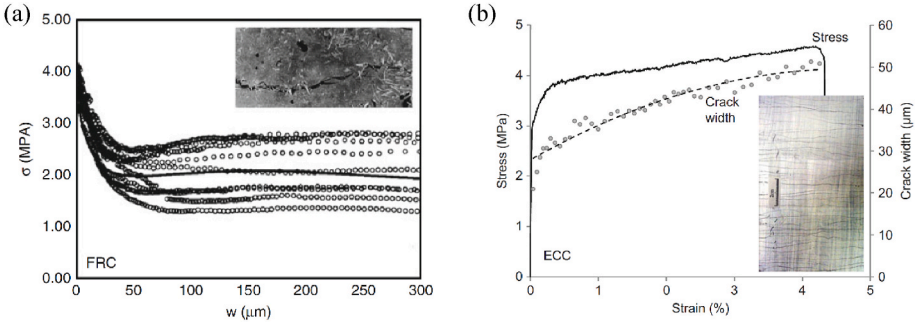

Fig. 1. Characteristics of different mechanical responses: (a) Tension-softening in FRC. The tensile load continuously drops to zero as the crack width reaches about half the fiber length of 12 mm. (b) Tensile strain-hardening of ECC (containing 2% volume fraction of PVA fibers). Load-bearing capacity is maintained under high strain of several percent, with width of multiple cracks limited to below 60 μm [10].

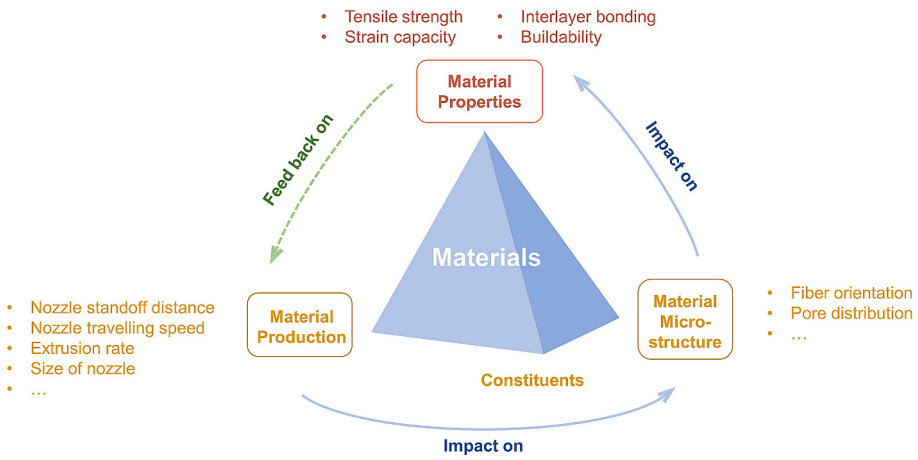

Fig. 2. Interrelated material indices.

Table 1
Chemical compositions of binders (%).

Binder	SiO_2	CaO	Al_2O_3	Fe_2O_3	MgO	SO_3	K_2O	TiO_2	L.O.I.
OPC	17.48	65.16	5.46	2.51	2.38	2.86	–	–	4.15
FA	41.12	6.05	37.00	5.56	0.88	1.08	0.71	1.38	2.89
SF	85.86	1.80	1.03	3.09	2.06	–	1.03	–	–

Note: OPC: ordinary Portland cement; FA: fly ash; SF: silica fume; L.O.I.: loss on ignition at 950 °C.

Table 2
Properties of PE fibers.

Density (g/cm^3)	Diameter (μm)	Length (mm)	Tensile strength (GPa)	Elastic modulus (GPa)	Elongation at break (%)
0.97	24	12	3.0	116	1–3

Table 3
Mix proportions (ingredient-to-binder weight ratios) of PE-ECC.

	OPC	FA	SF	Sand	Water	SP	PE Fiber
Mix-1	0.47	0.44	0.09	0.29	0.22	0.0010	0.010
Mix-2	0.47	0.44	0.09	0.29	0.24	0.0018	0.010

Note: SP: superplasticizer; binder = OPC + FA + SF.

illustrates the general processing procedure for printable PE-ECC.

2.2. Printing setup

The gantry-type 3D printer shown in Fig. 4a has three degrees of freedom. Along the slide rails in three orthogonal directions, the hopper storing ECC can be moved to prescribed position with the aid of computer. ECC is extruded out of the hopper under the action of gravity and with the force applied by a built-in cavity pump. Connected to the hopper is a circular nozzle with a diameter of 20 mm for material to get through. The extrusion rate of material, i.e., the volume flow, is primarily determined by the rotating speed of the cavity pump. While the travelling speed of nozzle is independently controlled and adjusted by computer program.

Two printing parameters posing substantial impact on printing process and quality, i.e., nozzle travelling speed and standoff distance, were chosen as the research foci. As schematically shown in Fig. 4b, nozzle travelling speed characterizes how fast the nozzle moves along the printing direction. It is essential to reconcile the travelling speed of nozzle with the extrusion rate of material. Excessively rapid travelling relative to extrusion rate may cause geometric defects in the extruded cross-section [3,17], while improperly slow deposition may accumulate redundant materials, impairing geometric integrity and structural stability. In addition, layer cycling time of printing will be stretched by slow printing, promoting so-called “cold joint”, where the deposited material loses its ability to establish a tight bond with the next layer of

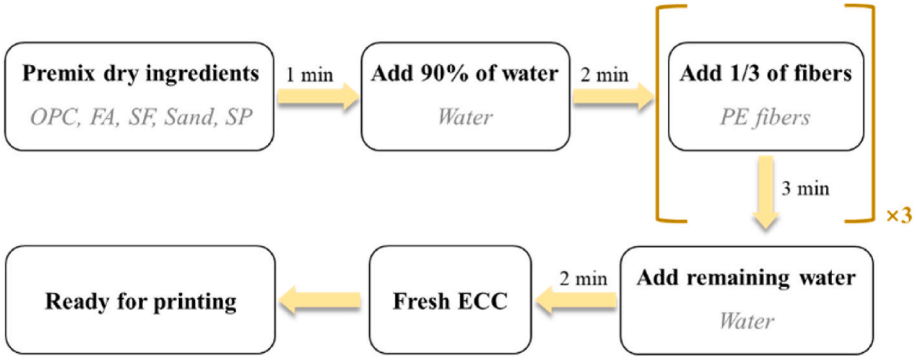

Fig. 3. Mix procedure for printable PE-ECC.

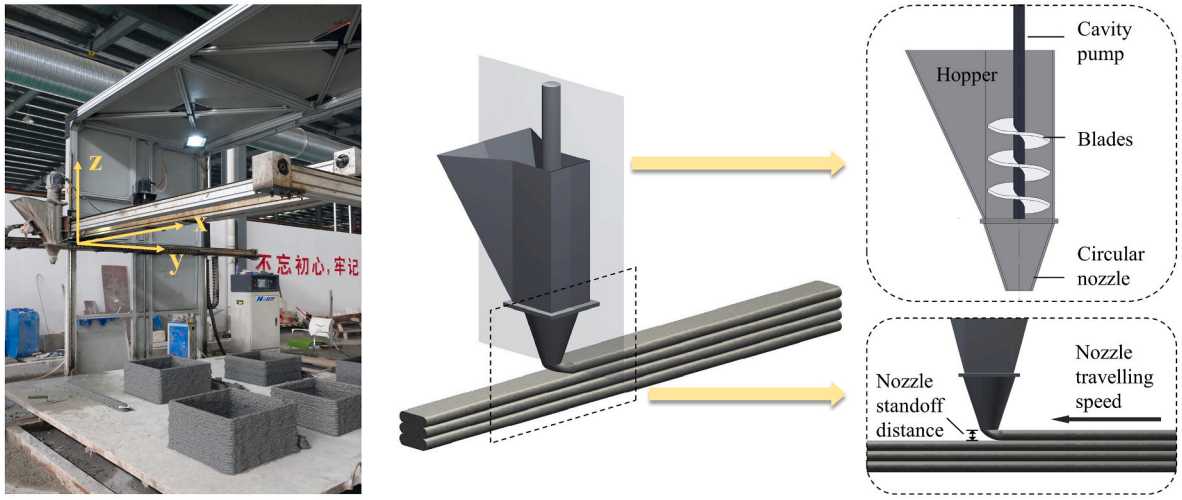

(a) Gantry printer (b) Schematic diagram of printing setup

Fig. 4. Printing setup.

wet material [24]. To investigate how the synchronization between movement speed and extrusion rate is achieved, extrusion rate was held constant by fixing the rotating speed of pump to 90 rpm in this experiment, and travelling speed was modulated to have three grades, i.e., 7, 8, and 9 m/min, namely low, standard and high speed, respectively.

As a predetermined parameter in control system, nozzle standoff distance describes a fixed vertical height by which the nozzle is elevated after one layer of printing. It is worth noting that the standoff distance defined here is not always equal to the thickness of layer or the height difference between nozzle and the top surface of a previous layer. Rather, it stays unchanged during the whole printing process. Previous researches suggested that reducing the standoff distance to approximately or below the filament thickness suppresses the appearance of large voids at the interface [22–24]. In this experiment, the highest standoff distance, i.e., 14 mm, is slightly lower than the height of a single undisturbed filament at 16 mm.

The printing parameter matrix is summarized in Table 4. The ID of each group indicates the travelling speed and standoff distance. For instance, H12 represents high travelling speed (H) and standoff distance of 12 mm.

2.3. Rheological test preparation

The time-evolving rheological properties of printing material are often the most decisive factors for 3D printing [17]. Successful printing must balance the conflicting requirements of flowability and buildability of fresh ECC. On the one hand, the initial fluidity of the fresh mixture should be adequate to smoothly extrude the material through the nozzle and simultaneously avoid clogging. On the other hand, the material should have a proper rigidity to bear its own weight and increasing vertical deadweight load (with additional printed layers) once extruded with no further support by the nozzle. To achieve this goal, the extruded material needs to exhibit sufficient shape retention ability and stability. This requires the properties of the printing ink to be delicately designed and harmoniously tuned to allow suitable rheological changes from mixing to filament placement and hardening.

Table 4
Printing parameter matrix.

Group ID	Nozzle travelling speed (m/min)	Nozzle standoff distance (mm)
S10	8	10
S12		12
S14		14
H12	9	12
L12	7	12

Note: S: standard travelling speed; H: high travelling speed; L: low travelling speed.

Flowability of printing ink is crucial for extrusion. Proper flowability enhances the ease, continuity and stability to extrude well-controlled filament through a nozzle [27]. In this research, flow table test was conducted to assess the flowability of PE-ECC in fresh state as per ASTM C1437 [28]. The fresh mixture was filled into an inverted half cone with a bottom diameter of 100 mm and a height of 60 mm. After removal of the cone, the table was raised and dropped 25 times. Then the diameter of the spread material was measured in two dimensions and the height reduction was regarded as slump, as shown in Fig. 5. The flowability of material was tested from 20 min to 80 min after water addition at intervals of 20 min to depict the time-dependent evolution of rheology.

Buildability is generally characterized as the ability of the printable material to build up without significant deformation or collapse [17,29]. The most straightforward approach to evaluate buildability is to compare the maximum height of printed element that can be built without failure under the same print settings [30]. Nonetheless, PE-ECC in this research exhibits remarkable resistance to material failure during structure buildup and satisfying structural stability with the geometries specified in this research. In this case, without failure of printed

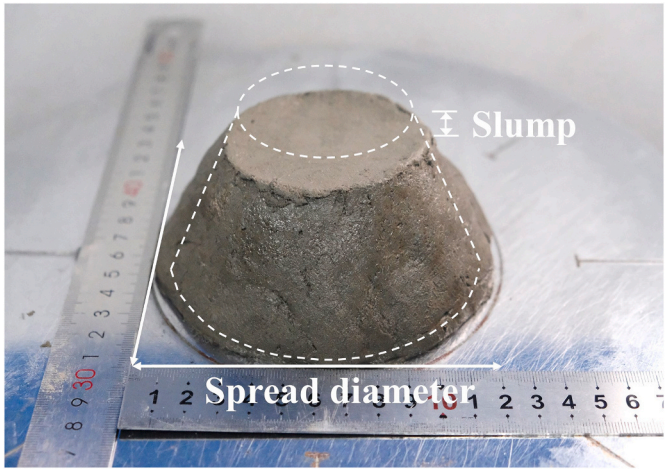

Fig. 5. Measurements in flow table test.

elements, resistance of the deposited material to deformation under increasing deadweight loading is considered as an appropriate indicator of buildability evaluation. This shape retention ability can be quantified by monitoring the geometrical changes of the printed filament and structure [31,32]. At the scale of an integrated printed object, average vertical strain is considered as an evaluation index [32]; while at the scale of single filament, variation of filament thickness can serve as a measure. In this experiment, a box-shape element stacking to approximately 300 mm high was printed for each group. The height of the whole element and each layer were measured at four edges separately and arrived at an average value.

2.4. Mechanical test preparation

2.4.1. Uniaxial tensile test

To prepare specimens for tensile test, a beam-like element with three parallel filaments per layer and five layers stacked was printed for each group and cured for 28 days. Dog-bone specimens [33] were then extracted directly from the beam-like element by saw cutting, as shown in Fig. 6a. Meanwhile, control specimens were prepared by mold casting and shared the same mix proportion with the printed ones. The geometry of dog-bone specimen is designed to promote dense micro-cracking in the narrow gauge region (80 mm in length). The specimens were uniaxially loaded at a fixed loading rate of 0.4 mm/min whilst two linear variable displacement transducers (LVDTs) measured the average tensile strain in the gauge region. Pin end shown in Fig. 6b helped to minimize misalignment and undesired moment during loading.

2.4.2. Interfacial fracture test

Layer interface is usually a weak link in 3DP due to potential high interlayer porosity and cold joint, therefore inducing inferior mechanical performance at the interface than that in the bulk material. For ECC, this is especially the case, since the lack of fiber bridging at the interface accentuates the anisotropy. Characterizing layer adhesion of 3DP-ECC is hence of paramount significance. Considering the failure of the interface is governed by crack propagation, three-point bending tests of notched specimens are appropriate for capturing interlayer bonding characteristics.

The specimens of interfacial fracture tests, with a dimension of 200 mm × 40 mm × 20 mm [34], were cut from the top portion of the printed box-shape elements at an age of 28 days, as shown in Fig. 7a. For each group, the specimens were notched either at the position of interface (namely inter-layer) or in the middle of a layer (namely intra-layer). The height of the notch is 40% of the beam depth, i.e., 16 mm. The setup for three-point bending test is shown in Fig. 7b. The loading above the notch was applied at a rate of 0.05 kN/s until specimen failure.

2.5. Micro-scale test approach

It is widely acknowledged that the mechanical properties of ECC at macro scale is dominated by its micro-structure, including features of fiber orientation and pore size and distribution [12,35], which is also applicable to 3DP-ECC. Changes in printing parameters are expected to introduce variations to the micro-structure of ECC.

Micro computed tomography scanner (μ-CT) was applied to observe the micro-structure of 3DP-ECC. μ-CT sliced and scanned the 3DP-ECC sample. By combining the sliced images, the 3D model of pores and dense bulk material was reconstructed and visualized in the software Dragonfly. Additionally, the feature and distribution of pores were captured and analyzed.

3. Results and discussions

3.1. Rheological properties

3.1.1. Flowability and extrudability

Fig. 8a plots the test data of flowability from 20 min to 80 min after water addition. Fresh mixture of Mix-2 outperformed that of Mix-1 in terms of spread diameter, indicating superior flowability. At a nozzle travelling speed of 8 m/min and a pump rotation rate of 90 rpm, the extrudability of Mix-1 appeared unsatisfactory. As shown in Fig. 8b, the relatively lower flowability of Mix-1 mixture resulted in difficulties in extrusion and deposition, leading to apparent surface cracks and undesired voids in printed filaments. Such defects in manufacturing could raise the risks of undermined structural integrity and inconsistent mechanical performance. In contrast, Mix-2 yielded continuous and intact filaments within open time. Ample fluidity assisted in the smooth extrusion of fresh ECC.

Considering the intrinsic conflict between sufficient flowability and desired buildability, the material must be harmoniously tuned to control its rheological properties. For a printing setup with cavity pump directly forcing the material out of a hopper, ECC Mix-2 is appropriate to enable successful extrusion whilst demonstrating shape retention ability.

3.1.2. Buildability

Intuitively, buildability describes the ability of the printed structure to be built up without failure. In the present research, buildability of 3DP-ECC was demonstrated by five groups of box-shape elements (Fig. 9) printed without any local buckling, overall collapse, excessive deformation or sensible eccentricity. More specifically, buildability can be quantified and evaluated by defining shape retention ability. Under

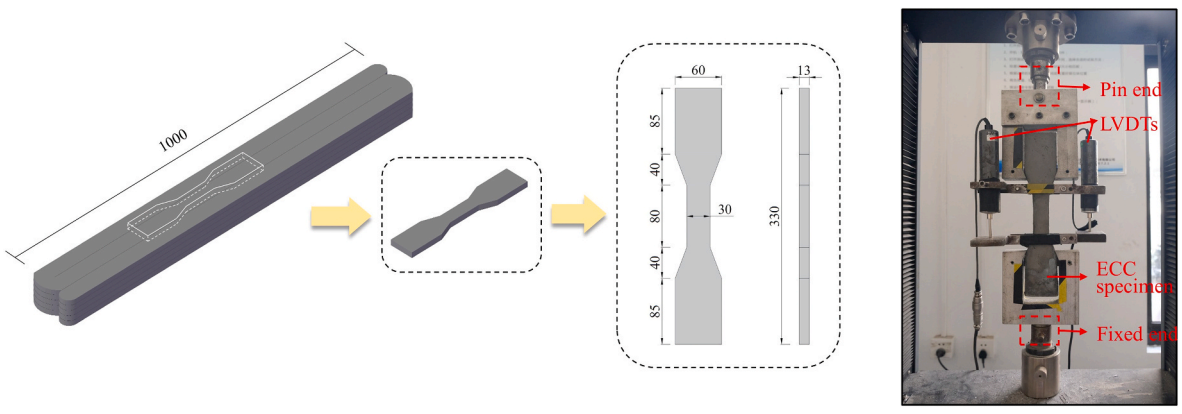

(a) Specimen configuration (b) Test setup

Fig. 6. Tensile specimen and test setup (Unit: mm).

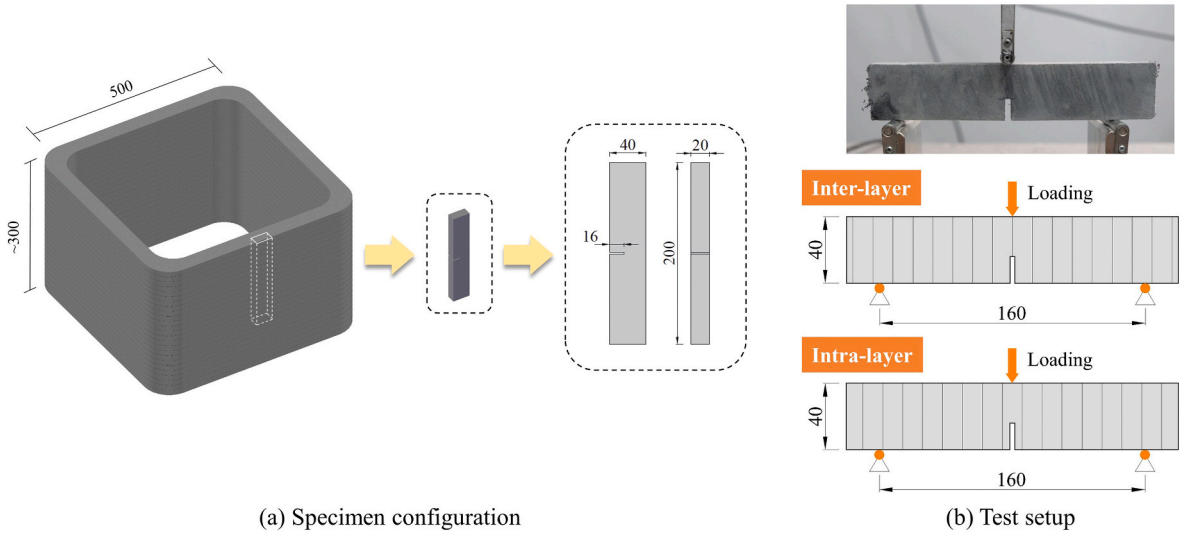

Fig. 7. Interfacial fracture specimen and test setup (Unit: mm).

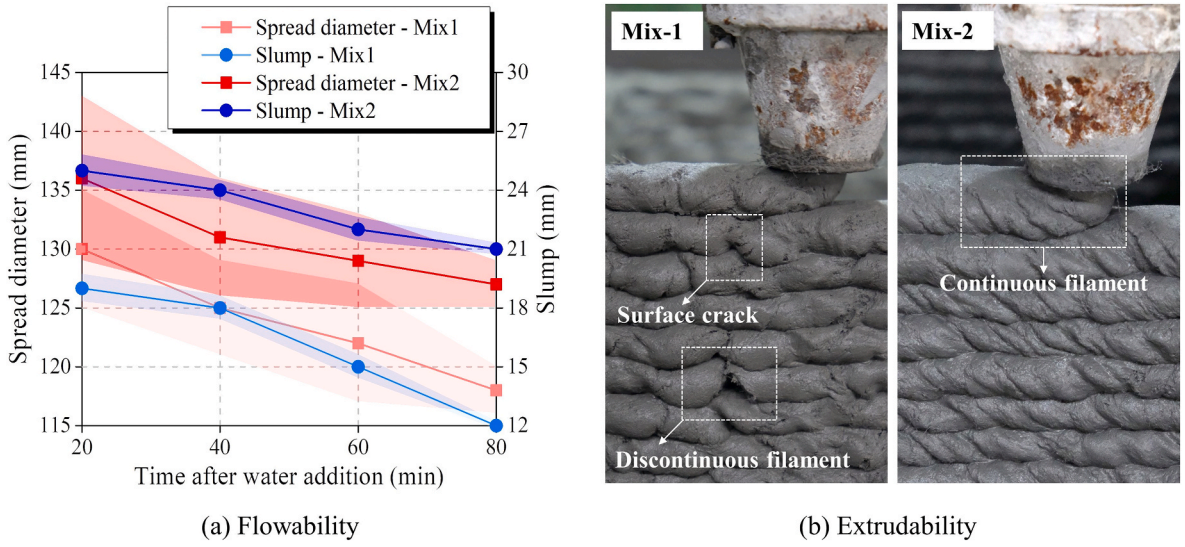

Fig. 8. Rheological properties of fresh printable ECC. The variability of measured spread diameter and slump is indicated by the shaded area in the plot.

the increasing load from upper layers and potential pressure applied by the nozzle, the filament deposited first inevitably undergoes a change in its cross-sectional shape. The magnitude of this geometrical change can be used to characterize buildability in 3DP and is especially straightforward for comparative research.

To capture the geometrical change at both the element-level and filament-level, the heights of the entire printed component (Table 5) and each layer were recorded. To enhance the comparability, the total height of all elements was controlled to around 300 mm during printing, except for S14 group with notably thicker layers. Without gravity-induced

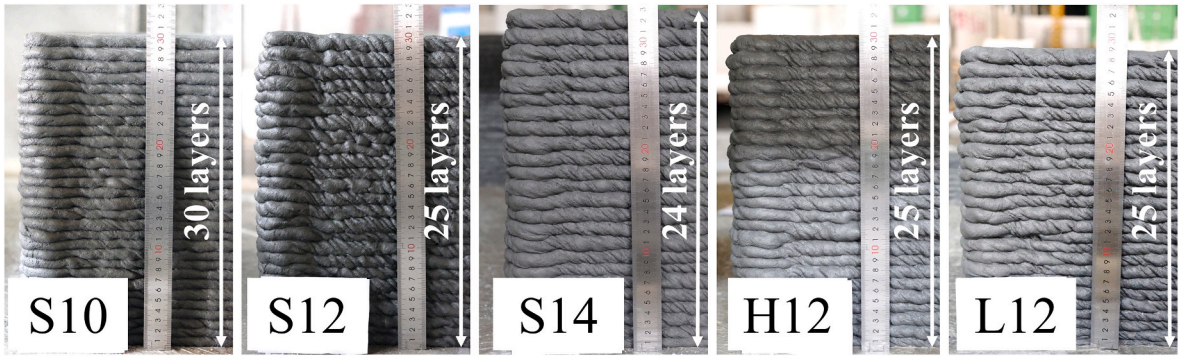

Fig. 9. Side views of the printed box elements.

deformation, the designed height of every element is supposed to be the product of layer number and nozzle standoff distance. Hence, the average vertical strain (Eq. (1)) of the printed elements can be calculated as one indicator of overall deformation. It should be noted that the influence of the top (h_1) and bottom (h_n) layer is removed to mitigate the interference caused by leveling and measurement errors.

$$\varepsilon_v = 1 - \frac{(H - h_1 - h_n)}{(n-2)\ h_0} \tag{1}$$

where ε_v represents the average vertical strain overlooking the top and bottom layer, n is the number of layers, h_0 is the prescribed nozzle standoff distance, H is the total height of the printed element, h_1 and h_n are the measured thickness of the top and bottom layer, respectively.

Generally, the average vertical strain scales with nozzle standoff distance (Fig. 10). As aforementioned, the nozzle standoff distance is slightly lower than the thickness of an undisturbed filament and therefore poses restriction on the vertical height of filament during extrusion. When fresh mixture leaves the outlet of the nozzle, a vertical pressure generated by the nozzle is exerted on the upper surface of the filament. Consequently, the fresh ECC filament is vertically compacted, decreasing in height and expanding laterally. This tendency increases as the standoff distance is lowered. A flatter cross-section of filament is then shaped. In this case, the load transfer between two adjacent layers occurs on a larger and flatter contact surface, thereby mitigating the effect of the gravity-induced pressure on causing further deformation of the filament. This "pre-loading" by nozzle in fact consumes part of the deformation capacity of the material in advance, so that upon completion of deposition, the filament retains little deformability but gains better shape retention ability. As a result, printing with a lower nozzle standoff distance improves the buildability of 3DP-ECC by yielding a less significant vertical strain.

Slightly higher travelling speed does not have a significant effect on the overall vertical strain, whereas the low printing speed shows a negative impact on buildability of 3DP-ECC. With slow movement of nozzle, redundant material accumulates behind the nozzle, reflected as a higher average filament width compared with the standard group. Excessive materials threaten the stability of geometrical dimensions, since it is difficult to control the position of material accumulation and the direction of material movement under compression. As a result, the layered materials may not stack neatly with control but skew among layers. This increases the vertical deformation and also impairs the dimensional precision and geometric stability of the printed object.

In addition to overall vertical strain of the object, variation in layer thicknesses can serve as an indicator of buildability as well. Deviation of layer thickness implies relative deformation among non-uniform layers. Compared with normalized average deformation, the deviation of layer thickness depicts more details about the vertical deformation distribution among different layers. As shown in Fig. 11, the standard deviations follow a similar trend with average vertical strain. The variation in layer thickness is enlarged with the increase of nozzle standoff distance, indicating more notable difference in deformation between the upper and lower materials. As an indirect shape index, the standard deviation of layer thickness is deemed as an auxiliary evaluation method and a supplement to the average vertical strain index.

Table 5
Geometrical dimensions of the printed box elements.

Group ID	Number of layers n	Height H (mm)	Ave. layer height $\overline{h}$ (mm)	Ave. filament width $\overline{w}$ (mm)
S10	30	302	9.96	42.0
S12	25	300	11.91	39.0
S14	24	332	13.77	37.0
H12	25	300	11.91	36.5
L12	25	294	11.87	40.0

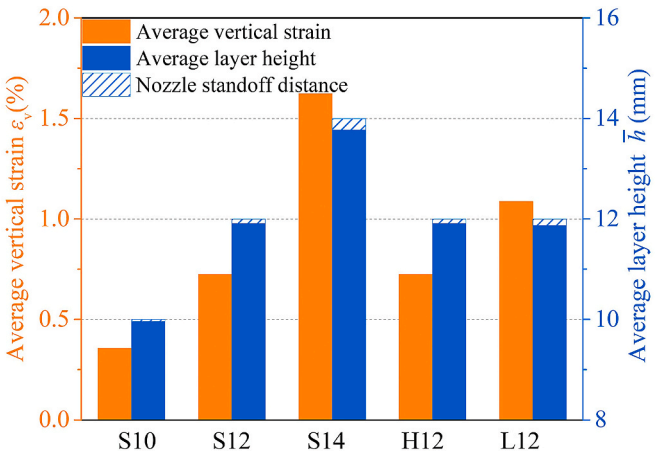

Fig. 10. Average vertical strain of the printed elements as influenced by nozzle standoff distance and nozzle travelling speed.

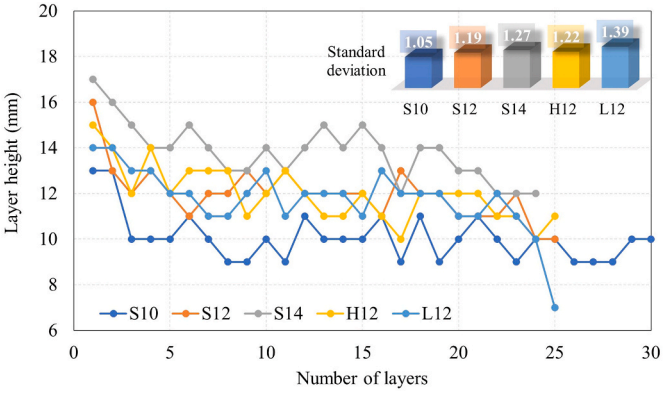

Fig. 11. Deviation of layer thickness.

3.2. Mechanical properties and micro-structures of 3DP-ECC

3.2.1. Tensile performance

By exhibiting strain-hardening behavior under tension, cast ECC offers unparalleled tensile performance in the field of cementitious materials. Although processed with an entirely different technology, 3DP-ECC is expected to exhibit similar ductility. Superior tensile performance in 3DP-ECC has been captured in previous studies [11,12,14,36]. Nonetheless, printing device and process parameters can pose dramatic influence.

In the current study, 3D printing process was observed to weaken the tensile performance of PE-ECC. As can be seen in Figs. 12 and 13, the cast specimens outperformed printed ECC in terms of multiple cracking ability, tensile strength and strain capacity. Both factors of fiber and matrix are responsible for the performance reduction in printing.

The observed discrepancy in tensile performance between cast and 3D printed specimens stems from the disturbance of fibers by the progressive cavity pump before extrusion. When the blades of the pump rotate, fresh ECC is continuously sheared in the hopper and extruded out of the nozzle in a twisted form. In this process, the thin synthetic fibers are vulnerable to curling considering their flexibility. The crack-bridging ability of fibers are therefore not fully exploited in resisting tension. Moreover, the orientation inside the twisted filament also appears to be not fully aligned with the printing direction. As shown in Fig. 14, fibers in the cast specimens are randomly distributed and orientated. However, fiber in printed ECC has a certain trend of orientation. The filament of S12 exhibits a fiber orientation that is approximately 45° oblique to the printing direction, which significantly

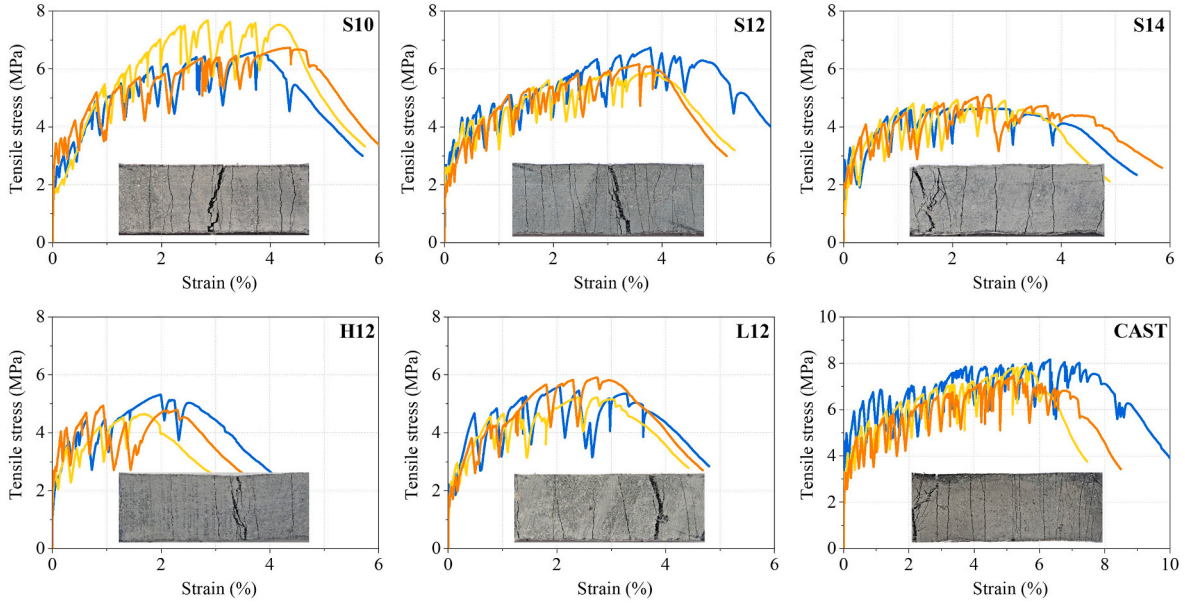

Fig. 12. Tensile stress-strain curves of 3DP-ECC and corresponding damage pattern after uniaxial tensile tests, compared to the cast specimens.

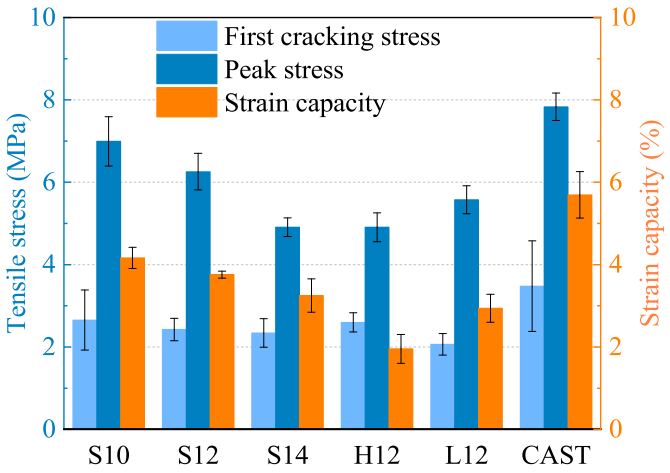

Fig. 13. Tensile performance of the printed and cast ECC.

weakens their tension resistant efficiency in the print direction. An even more obvious in-plane angle is observed in the L12 group. Due to the accumulation of redundant materials, the fibers are nearly orthogonal to the nozzle movement direction. This explains the less-than-desired tensile performance observed at low printing speed.

Pore structure also influences the tensile performance. In this study, porosity was measured by the software Dragonfly. It is generally expected that the print process results in a lower porosity than its cast counterpart since the extrusion pressure should compact the material [14,18]. However, this turned out not to be the case. Porosity by volume of the cast sample, as shown in Fig. 15a, is between those of S12 and S10 group. Nevertheless, the strength of the matrix as reflected by the initial cracking strength, is not only affected by porosity, but is strongly influenced by the pore size distribution. Compared with 3DP-ECC, cast ECC possesses a higher proportion of finer pores (Fig. 15b), indicating a more refined micro-pore structure. Therefore, cast ECC showed a higher initial cracking strength under tension due to its denser matrix.

The standoff distance of nozzle imposes notable influence to the tensile performance of 3DP-ECC. Enhanced tensile performance is seen accompanied by a lower standoff distance. This improvement can be viewed from two aspects: fiber and matrix. At a lower standoff distance, the additional compressive stress applied by the nozzle flattened the fiber and increased its alignment in the horizontal plane. That is, the out-of-plane angle of the fiber is reduced. In this case, the tensile capacity in the print direction is improved due to more efficient fiber orientation. On the other hand, due to the additional stress by the nozzle, the material undergoes a secondary compaction after deposition, and the pore structure is slightly affected. Lower standoff distance yields denser matrix with lesser porosity, as indicated in Fig. 15a. It can also be seen from Fig. 13 that the initial cracking stress of ECC scales inversely with

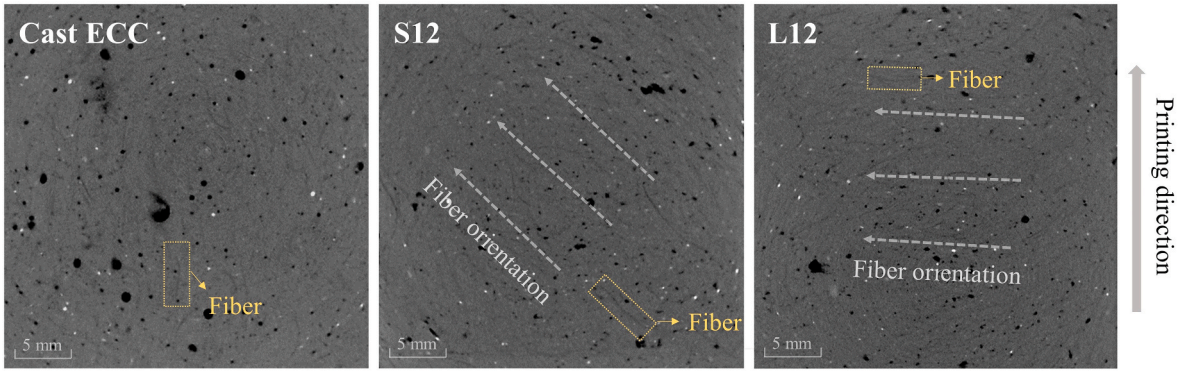

Fig. 14. Fiber orientation in μ-CT scanning images for cast versus 3D printed (S12 and L12) specimens.

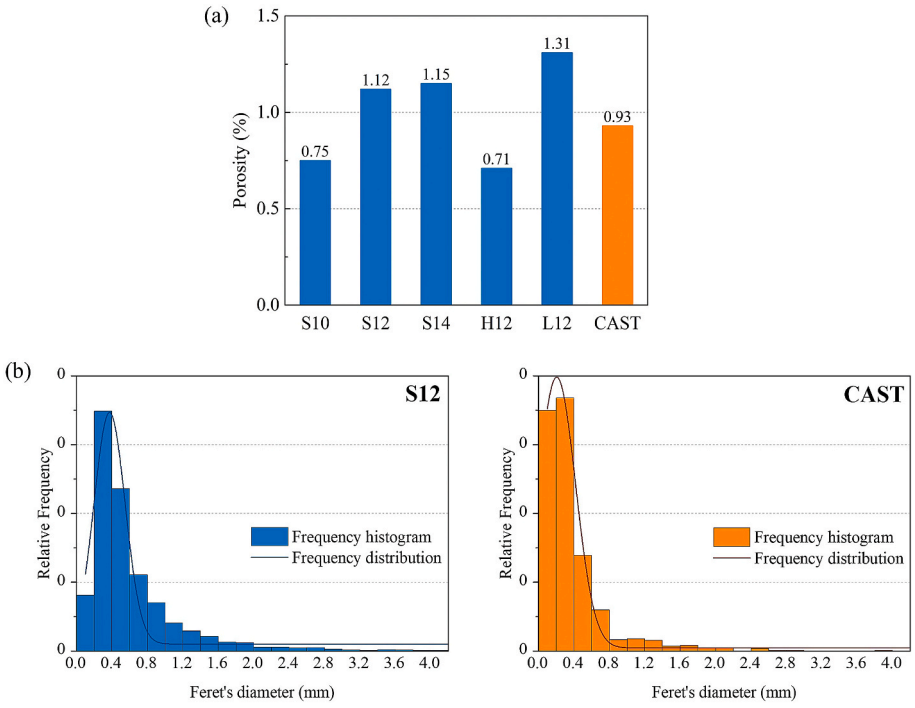

Fig. 15. (a) Porosities and (b) pore size distribution of the printed and cast ECC.

nozzle standoff distance in general, confirming the reduction of porosity and toughening of matrix. Taken the effects of fiber and matrix together, reducing the nozzle standoff distance from 14 mm to 10 mm increased the strain capacity of the same mixture by approximately 30%, while the tensile strength was enhanced by up to 39%.

Regarding nozzle travelling speed, moderate printing speed, i.e., the S12 group, showed superior tensile capacity than both H12 and L12 groups, indicating printing speed may be optimized to yield optimal tensile performance. One underlying issue associated with low printing speed is the potential accumulation of excessive materials. With limited space for deposited material, the newly-extruded redundant material will compress the former, having fibers more likely aligned orthogonal to printing direction (Fig. 14). For high-speed printing, despite the compactness of the matrix (Fig. 15a), the tensile performance demonstrated in the tests cannot be kept on par with the S12 group. One possible explanation is that the extruded filaments of H12 are thinner than standard ones because of the relatively small material volume flow. As a consequence, H12 also experienced a relatively smaller vertical secondary compaction caused by the additional stress of the nozzle. Greater out-of-plane angles of fibers are therefore formed, leading to a weakening of the tensile performance.

3.2.2. *Interfacial bonding*

Interfacial bonding of 3DP-ECC originates from two major sources. One part of layer adhesion is generated in the contacting area of wet cementitious materials, and closely associated with layer cycling time. It is natural to expect that printing speed imposes notable influence on the formation of cold joint. In this research, however, the maximum difference in single-layer printing time was restrained to less than 4 s due to the limited contour length. Therefore, printing speed is not considered to be a main factor affecting matrix adhesion. The other portion of interfacial bonding comes from fibers bridging the interface when it is torn apart. When an upper layer of material is deposited, the self-weight will press it into the underlying layer, with part of the fibers penetrating through the interface and yielding inter-layer fracture resistance.

The superimposed influence of these two sources shapes the typical interfacial fracture curve as a dual-peak curve (Fig. 16). During the three-point bending, load first increased almost linearly with displacement until the fracture toughness of the matrix was exhausted. The brittle fracture of the matrix caused a rapid post-peak drop of load. Nonetheless, the load would not plummet to zero as in the failure of brittle cementitious materials. Due to the existence of fibers, stress redistributed after the matrix fractures, and fibers bridging the fractured surface played a crucial role in bearing the load. In this case, the load capacity rose halfway until it reached another peak or a plateau, and allowed further development of large deflection. The second ascending branch characterizes the fiber bridging ability of ECC, and the enhancement in overall fracture resistance capacity is remarkable. Compared with the brittle fracture of traditional cementitious materials, the ductile failure exhibited by 3DP-ECC substantially delays the occurrence of failure and minimizes the hazard caused by catastrophic failure.

Fiber is the main factor responsible for the difference of fracture resistance between inter- and intra-layer samples. As shown in Fig. 17, fiber bridging inside the printed layer is generally more pronounced, attributed to the advantage in fiber quantity. As a result, the fracture resistance of intra-layer samples is mostly superior to that of inter-layer ones (Fig. 18). Nonetheless, due to the significant cross-sectional deformation of the filament in the S14 group, as will be detailly discussed in later paragraph, the interface of the wet material is strongly bonded, and the unevenness of the interface may increase. This promotes the fracture resistance at the interface, but also causes potential difficulties in accurately positioning the interface when notching, which may explain why the inter-layer samples of S14 group exhibit higher residual loads than those of intra-layer ones (Fig. 18).

Compared with fiber, matrix is not the dominant factor accounting for the difference. Through μ-CT scanning, pore distribution along layer stacking direction was observed. It turned out that the porosity in inter-layer area does not show prominent differences with intra-layer ones (Fig. 19). More air voids are introduced to the interior of bulk material due to the agitation of pump than the interface. The pore distribution also confirms that having the nozzle standoff distance slightly lower than the natural filament height can effectively suppress the appearance of interlayer voids, since it is natural to anticipate air voids entrained

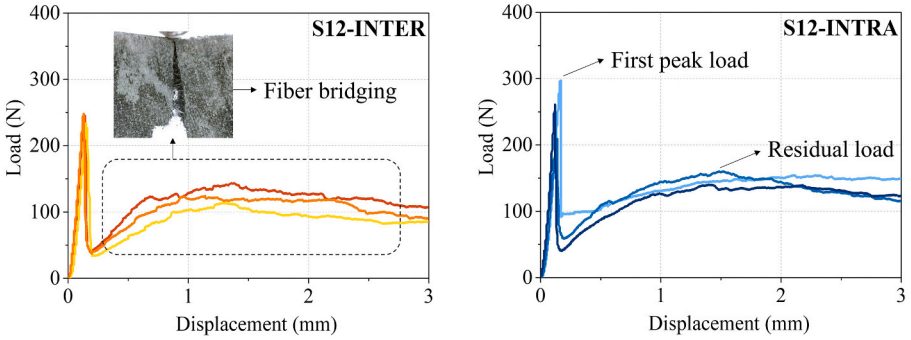

Fig. 16. Ductile inter- and intra-layer failure demonstrated by 3DP-ECC.

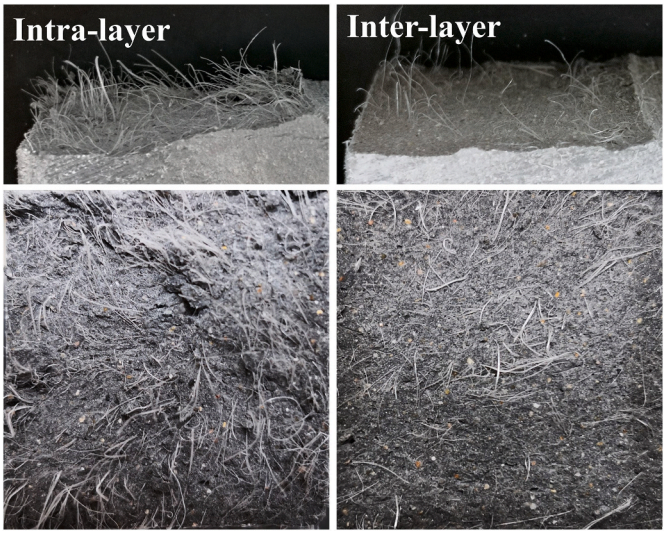

Fig. 17. Fracture surfaces of intra- and inter-layer samples.

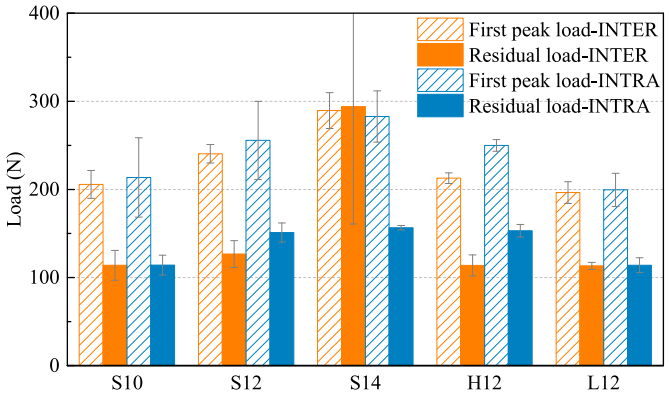

Fig. 18. Fracture resistance capacity of 3DP-ECC.

between the layers to form large voids [37].

As presented in Fig. 18, both inter-layer and intra-layer fracture resistance capacity scales with nozzle standoff distance. This remarkable trend is related to the amount of fibers bridging adjacent layers, which is further associated with the deformation of the contacting region. Greater nozzle standoff distance (e.g., S14) generally leads to more significant cross-sectional deformation. Since the original shape is barely disturbed by the additional pressure applied by the nozzle, the filament is able to maintain its cross-sectional geometry similar to the nozzle shape (circular) when extruded. Nonetheless, due to the inevitable dead-weight loading from the upper layers, the material is vertically squeezed to experience geometrical change, and the contacting area of adjacent layers is expanded, as illustrated in Fig. 20. During this deformation process, the fibers near surface penetrate into the cement matrix of the adjacent layer, contributing to interfacial fracture resistance. Interlayer bonding is therefore strengthened. In contrast, a lower nozzle standoff distance generates a less rounded cross-section when extruded. Synchronous deformation between the two layers is relatively imperceptible. In addition, more fibers are flattened and aligned along the horizontal plane, meaning less fibers penetrating the interface, and leading to weaker interfacial fracture resistance.

It is worth noting that for different nozzle standoff distances, the in-plane tensile performance and interfacial bonding always show opposite trends, as shown in Figs. 13 and 18. This is because the nozzle height and the additional vertical stress primarily determine the shape and remaining deformability of the filament. Lower nozzle height means more preloading, more horizontal fiber orientation, which brings about excellent in-plane tensile characteristics but yields weaker interfacial bonding.

Variation in printing speed, at least within the range in the current study, does not significantly alter the interfacial fracture resistance, as confirmed by the similar residual loads of the INTER groups of S12, H12 and L12 in Fig. 18.

4. Conclusions

This research experimentally investigates the influence of two printing parameters – nozzle travelling velocity (print speed) and nozzle standoff distance – on the micro-structure and mechanical performance of 3DP-ECC. The following conclusions can be drawn:

1. In order to capture geometrical changes at both the element-level and filament-level, average vertical strain and variation in layer thickness are suggested to be adopted as quantitative indicators for evaluating buildability of 3DP-ECC. Experimental evidences showed that the buildability of 3DP-ECC scales inversely with nozzle standoff distance and could be undermined by slow printing.
2. The tensile performance of 3DP-ECC was weakened by printing when compared to its cast equivalent, indicated by 10% and 26% reductions in tensile strength and strain capacity, respectively. The primary reason is disturbed fiber orientation inside the twisted filament and different pore distribution.
3. The tensile properties of 3DP-ECC were enhanced by lower standoff distance and moderate printing speed. Nozzle standoff distance mainly poses effect by altering the out-of-plane angle of fibers and the micro-pore structure of matrix, while printing speed also exerts influence on the in-plane orientation and out-of-plane angle of fibers.
4. Inter-layer bonding of 3DP-ECC was found to be strengthened by greater nozzle standoff distance. More fibers take effect in connecting adjacent layers when significant cross-sectional deformation happens along with greater nozzle standoff distance. Nonetheless,

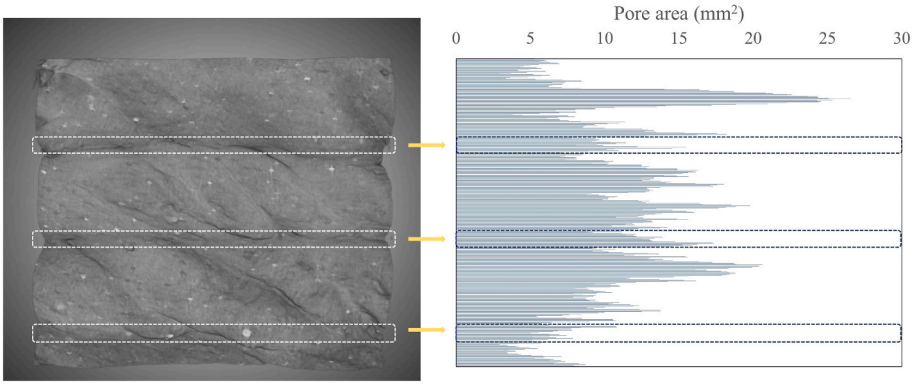

Fig. 19. Pore distribution along vertical direction (the boxed areas represent interfaces).

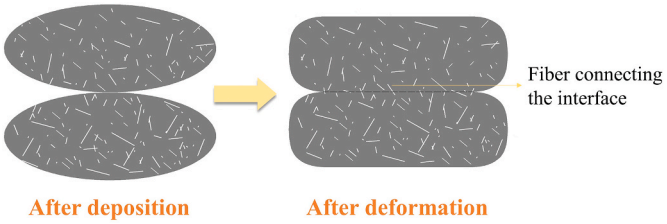

Fig. 20. Geometrical change in filament cross-sections after filament deposition.

different printing speed does not notably alter the bridging effect of inter-layer fibers.

Printing parameters and material properties are important indicators that are intrinsically linked in 3DP practice. In this research, significant trends in material performance caused by different printing parameters have been captured. However, the same change of printing parameters can lead to trade-offs for different properties. For example, reduction of nozzle standoff distance can considerably improve the tensile performance of 3DP-ECC, but simultaneously impair the interfacial fracture resistance. Therefore, a cautious selection of printing parameters is warranted.

Overall, this research portrays the interaction between printing parameters and material properties as a cornerstone for optimal 3DP process. Through comprehensive and in-depth research, the performance of 3DP-ECC can be enhanced and optimized by careful adjustments of the printing parameters. Correspondingly, the properties of the finished product can also be used as feedbacks to provide valuable information and guidance for the optimization of printing parameters. In this manner, additive manufacturing of ECC when fitted with real-time sensing capability (for example, of printed layer thickness), can create a closed-loop 3DP process control (for example of standoff distance).

Authorship contribution statement

Wen Zhou: Methodology, Investigation, Validation, Writing - Original Draft. **Yamei Zhang**: Supervision, Validation, Writing - review & editing. **Lei Ma**: Investigation. **Victor C Li**: Conceptualization, Supervision, Validation, Writing - review & editing.

Declaration of competing interest

The authors declare that they have no known competing financial interests or personal relationships that could have appeared to influence the work reported in this paper.

Acknowledgments

Financial support of this research is provided by the University of Michigan MCubed 3 Program, the Center for Low Carbon Built Environment (CLCBE) and the James R. Rice Distinguished University Professorship. W. Zhou is supported by a University of Michigan fellowship for graduate studies.

References

[1] G. De Schutter, K. Lesage, V. Mechtcherine, V.N. Nerella, G. Habert, I. Agusti-Juan, Vision of 3D printing with concrete — technical, economic and environmental potentials, Cement. Concrete. Res. 112 (2018) 25–36.
[2] M.K. Mohan, A.V. Rahul, G. De Schutter, K. Van Tittelboom, Extrusion-based concrete 3D printing from a material perspective: a state-of-the-art review, Cement Concr. Compos. 115 (2021), 103855.
[3] R.A. Buswell, W.R. Leal De Silva, S.Z. Jones, J. Dirrenberger, 3D printing using concrete extrusion: a roadmap for research, Cement. Concrete. Res. 112 (2018) 37–49.
[4] M. Gebler, A.J.M.S. Uiterkamp, C. Visser, A global sustainability perspective on 3D printing technologies, Energ. Pol. 74 (2014) 158–167.
[5] I. Agustí-Juan, G. Habert, Environmental design guidelines for digital fabrication, J. Clean. Prod. 142 (2017) 2780–2791.
[6] I. Agustí-Juan, F. Müller, N. Hack, T. Wangler, G. Habert, Potential benefits of digital fabrication for complex structures: environmental assessment of a robotically fabricated concrete wall, J. Clean. Prod. 154 (2017) 330–340.
[7] I. Perkins, M. Skitmore, 3D printing in the Construction Industry: a review, Int. J. Constr. Manage 15 (2015) 1–9.
[8] D. Asprone, C. Menna, F.P. Bos, T.A.M. Salet, J. Mata-Falcón, W. Kaufmann, Rethinking reinforcement for digital fabrication with concrete, Cement. Concrete. Res. 112 (2018) 111–121.
[9] V.C. Li, F.P. Bos, K. Yu, W. McGee, T.Y. Ng, S.C. Figueiredo, K. Nefs, V. Mechtcherine, V.N. Nerella, J. Pan, G.P.A.G. van Zijl, P.J. Kruger, On the emergence of 3D printable engineered, strain hardening cementitious composites (ECC/SHCC), Cement. Concrete. Res. 132 (2020), 106038.
[10] V.C. Li, Engineered Cementitious Composites (ECC), first ed., Springer, Berlin, Germany, 2019.
[11] K. Yu, W. McGee, T.Y. Ng, H. Zhu, V.C. Li, 3D-printable engineered cementitious composites (3DP-ECC): fresh and hardened properties, Cement. Concrete. Res. 143 (2021), 106388.
[12] B. Zhu, J. Pan, B. Nematollahi, Z. Zhou, Y. Zhang, J. Sanjayan, Development of 3D printable engineered cementitious composites with ultra-high tensile ductility for digital construction, Mat. Design 181 (2019), 108088.
[13] S.C. Figueiredo, C.R. Rodríguez, Z.Y. Ahmed, D.H. Bos, Y. Xu, T.M. Salet, O. Çopuroğlu, E. Schlangen, F.P. Bos, An approach to develop printable strain hardening cementitious composites, Mat. Design 169 (2019), 107651.
[14] H. Ogura, V. Nerella, V. Mechtcherine, Developing and testing of strain-hardening cement-based composites (SHCC) in the context of 3D-printing, Materials 11 (2018) 1375.
[15] W. McGee, T.Y. Ng, K. Yu, V.C. Li, Extrusion nozzle shaping for improved 3DP of Engineered Cementitious Composites (ECC/SHCC), in: F. Bos, S. Lucas, R. Wolfs, T. Salet (Eds.), Second RILEM International Conference on Concrete and Digital Fabrication, vol 28, Springer, Cham, DC 2020. RILEM Bookseries, https://doi.org/10.1007/978-3-030-49916-7_89.
[16] T. Wangler, E. Lloret, L. Reiter, N. Hack, F. Gramazio, M. Kohler, M. Bernhard, B. Dillenburger, J. Buchli, N. Roussel, R. Flatt, Digital concrete: opportunities and challenges, RILEM Tech. Lett. 1 (2016) 67–75.
[17] N. Roussel, Rheological requirements for printable concretes, Cement. Concrete. Res. 112 (2018) 76–85.

[18] T.T. Le, S.A. Austin, S. Lim, R.A. Buswell, R. Law, A.G.F. Gibb, T. Thorpe, Hardened properties of high-performance printing concrete, Cement. Concrete. Res. 42 (2012) 558–566.
[19] B. Panda, N.A.N. Mohamed, Y.W.D. Tay, M.J. Tan, Bond Strength in 3D Printed Geopolymer Mortar, RILEM International Conference on Concrete and Digital Fabrication, Zurich, Switzerland, 2018, pp. 200–206.
[20] E. Keita, H. Bessaies-Bey, W. Zuo, P. Belin, N. Roussel, Weak bond strength between successive layers in extrusion-based additive manufacturing: measurement and physical origin, Cement. Concrete. Res. 123 (2019), 105787.
[21] V.N. Nerellaa, M. Nätherb, A. Iqbala, M. Butlera, V. Mechtcherinea, Inline quantification of extrudability of cementitious materials for digital construction, Cement Concr. Compos. 95 (2019) 260–270.
[22] B. Panda, S.C. Paul, N.A.N. Mohamed, Y.W.D. Tay, M.J. Tan, Measurement of tensile bond strength of 3D printed geopolymer mortar, Measurement 113 (2018) 108–116.
[23] F. Bos, R. Wolfs, Z. Ahmed, T. Salet, Additive manufacturing of concrete in construction: potentials and challenges of 3D concrete printing, Virtual Phys. Prototyp. 11 (2016) 209–225.
[24] B. Panda, N.A. Noor Mohamed, S.C. Paul, G. Bhagath Singh, M.J. Tan, B. Šavija, The effect of material fresh properties and process parameters on buildability and interlayer adhesion of 3D printed concrete, Materials 12 (2019) 2149.
[25] R.J.M. Wolfs, F.P. Bos, E.C.F. van Strien, T.A.M. Salet, A Real-Time Height Measurement and Feedback System for 3D Concrete Printing, Springer International Publishing, Cham, 2017, pp. 2474–2483.
[26] J. Zhou, S. Qian, G. Ye, O. Copuroglu, K. van Breugel, V.C. Li, Improved fiber distribution and mechanical properties of engineered cementitious composites by adjusting the mixing sequence, Cement Concr. Compos. 34 (2012) 342–348.
[27] S. Lim, R.A. Buswell, T.T. Le, S.A. Austin, A.G.F. Gibb, T. Thorpe, Developments in construction-scale additive manufacturing processes, Automat. Constr 21 (2012) 262–268.
[28] ASTM C1437, Standard Test Method for Flow of Hydraulic Cement Mortar.
[29] M. Amran, H.S. Abdelgader, A.M. Onaizi, R. Fediuk, T. Ozbakkaloglu, R.S. M. Rashid, G. Muralih, 3D-printable alkali-activated concretes for building applications: a critical review, Construct. Built. Mater. 319 (2022), 126126.
[30] Y. Zhang, Y. Zhang, G. Liu, Y. Yang, M. Wu, B. Pang, Fresh properties of a novel 3D printing concrete ink, Construct. Built. Mater. 174 (2018) 263–271.
[31] T.T. Le, S.A. Austin, S. Lim, R.A. Buswell, A.G.F. Gibb, T. Thorpe, Mix design and fresh properties for high-performance printing concrete, Mater. Struct. 45 (2012) 1221–1232.
[32] G. Ma, Z. Li, L. Wang, Printable properties of cementitious material containing copper tailings for extrusion based 3D printing, Construct. Built. Mater. 162 (2018) 613–627.
[33] JSCE, Recommendations for Design and Construction of High Performance Fiber Reinforced Cement Composites with Multiple Fine Cracks, Japan Society of Civil Engineers, Tokyo, Japan, pp. 1–16.
[34] S.P. Shah, Determination of fracture parameters (K Ic s and CTODc) of plain concrete using three-point bend tests, Mater. Struct. 23 (1990) 457–460.
[35] M. Li, V.C. Li, Rheology, fiber dispersion, and robust properties of Engineered Cementitious Composites, Mater. Struct. 46 (2013) 405–420.
[36] J. Yu, C.K.Y. Leung, Impact of 3D Printing Direction on Mechanical Performance of Strain-Hardening Cementitious Composite (SHCC), RILEM International Conference on Concrete and Digital Fabrication, Zurich, Switzerland, 2018, pp. 255–265.
[37] V.N. Nerella, S. Hempel, V. Mechtcherine, Effects of layer-interface properties on mechanical performance of concrete elements produced by extrusion-based 3D-printing, Construct. Built. Mater. 205 (2019) 586–601.